# Direct numerical simulation of low-Prandtl number turbulent convection above a wavy wall

Orsola Errico, Enrico Stalio*

*Dipartimento di Ingegneria "Enzo Ferrari"*
*Università degli Studi di Modena e Reggio Emilia*
*Via Vignolese 905/B*
*41125 Modena - Italy*

---

**Abstract**

Turbulent forced convection is investigated by Direct Numerical Simulation in a channel with one sinusoidal wavy wall and one flat wall. Fluid flow and heat transfer are periodically fully developed, the simulated Reynolds number of the bulk velocity and the hydraulic diameter is $\mathrm{Re} = 18\,880$ while three Prandtl numbers are considered, *i.e.* $\mathrm{Pr} = 0.025$, $\mathrm{Pr} = 0.2$, and $\mathrm{Pr} = 0.71$. The fluid flow is characterized by separation, reattachment and a shear layer downstream the wave peak, these are conditions relevant for turbulent heat transfer and passive scalar transport applications.

In the range of Péclet numbers investigated, the most important heat transfer mechanism is by mean flow advection. Accordingly, the peak heat transfer region is in the upslope part of the domain. The separation bubble instead acts as a barrier to convection and the heat transfer rate is minimum close to separation. An *a priori* analysis is performed in order to assess the accuracy of turbulent heat transfer models based on the Generalized Gradient Diffusion Hypothesis.

*Keywords:* , Turbulent Convection, Periodically Fully Developed, Low Prandtl Number, Liquid Metal, Local heat transfer rate, Heat transfer in separated flow, Gradient Diffusion Hypothesis

---

*Corresponding author
*Email address:* `enrico.stalio@unimore.it` (Enrico Stalio)

## Contents

## Introduction

Liquid metals are used as coolants in many current nuclear reactors designs, but the heat transfer behavior of low Prandtl number fluids in conditions relevant to applications are still to be elucidated, also because of the difficulty in performing experiments. Turbulent heat transfer of liquid metals have to be investigated in conditions relevant for the applications *i.e.* in complex flow configurations, involving separation, reattachment and possibly shear layer regions. Only a deeper knowledge of these characteristics can allow for a more accurate turbulent heat transfer modeling to be employed in the design cooling systems which might ensure also passive safety.

A number of publications on turbulent convection in low Prandtl number flows consider the flat channel configuration. Kawamura and co-workers [1, 2] perform direct numerical simulations (DNS) in the flat channel case, the investigated Prandtl number values range between 0.025 and 0.71, while friction Reynolds numbers $\mathrm{Re}_\tau = 180$ and 395 are considered. The authors observe that the effect of Re on the turbulent Prandtl number is stronger at low Pr. Instead, for $\mathrm{Pr} > 0.2$ the near-wall value of turbulent Prandtl number is found to be about unity, independently of both Re and Pr. Piller *et al.* [3] present results of a DNS for the same range of Prandtl numbers as in [1, 2] and for $\mathrm{Re}_\tau = 150$. Based on temperature spectra and the correlations coefficient between velocity and temperature fluctuations, they observe that in low Prandtl number fluids the molecular conductivity acts as a filter, decreasing the effectiveness of large frequency velocity fluctuations in creating temperature fluctuations. Abe and co-workers [4] use DNS results to focus on the characteristics of surface heat flux fluctuations. Their simulations span a wide range of Re number; $\mathrm{Re}_\tau = 180$, 395, 640 and 1020 and $\mathrm{Pr} = 0.025$ and 0.71. The comparison between the space-time correlations at $\mathrm{Pr} = 0.71$ and 0.025 reveals that the surface heat flux fluctuations propagate downstream with a larger convection velocity for $\mathrm{Pr} = 0.025$, with respect to $\mathrm{Pr} = 0.71$.

There is a large volume of published studies investigating the effects of surface undulation on turbulent flow features, as the experimental works by Zilker and Hanratty [5], Hudson *et al.* [6, 7], Zenklusen *et al.* [8], and the numerical studies by Maaß and Schumann [9], Cherukat *et al.* [10], Calhoun and Street [11], Patel *et al.* [12].

Experimental and numerical studies of forced turbulent convection in wavy channels are also available in the literature, but only for order one Prandtl number fluids. Günther and von Rohr [13] conduct an experimental study on the same geometry and for the same Reynolds number as in Ref. [6]. They use a Liquid Crystal Thermometry (LCT) technique and detect the size of dominant spanwise scales of the fluid temperature by means of a POD. Digital Particle Image Velocimetry (PIV) and Planar Laser Induced Fluoresce (PLIF) technique are instead used by Kuhn *et al.* [8] to study the influence of wavy walls on the passive scalar transport in turbulent regime. They consider channels with one flat wall and a wavy wall of varying amplitude, for a Reynolds number based on half the average channel height $\mathrm{Re} = 11\,200$.

Numerical investigations using RANS models or LES for simulating turbulent heat transfer in wavy channels have also appeared in the literature. Dellil *et al.*[14] use a k-$\varepsilon$ turbulence model to study the turbulent flow and heat transfer over wavy walls. Waves of different amplitude are considered; they observe that while increasing $a/\lambda$ between 0 to 0.1, the average Nusselt number initially increases until a critical value is reached. Choi and Suzuki [15] perform LES of turbulent heat transfer in a channel with one wavy wall, for three different values of the wave amplitude in the range $0.01 \leq a/\lambda \leq 0.1$. The Prandtl number investigated is $\mathrm{Pr} = 0.71$ and the Reynolds number the same as in Ref. [6]. An instantaneous streamwise vortex is sometimes found in the upslope part of the wave, which enhances the local heat transfer rate. A DNS study has been performed by Rossi [16], for the usual wave steepness of $a/\lambda = 0.05$, and a Reynolds number based on the average channel height, $Re = 6\,850$ and Prandtl number $Pr = 0.71$. The results of this study have never been published in a journal, they instead have been used for comparison purposes in the later work by Rossi [17], where Reynolds Averaged Navier Stokes and scalar transport equations are used to evaluate the predictive capabilities of the algebraic heat-flux models in comparison to the simple gradient model. Rossi [17] reports that algebraic heat-flux models are able to improve the scalar field predictions in the analysis of scalar dispersion from a point source over the wavy wall.

The present work investigates the turbulent forced convection of low to order one Prandtl number fluids for flow configurations relevant for heat exchangers passages, *i.e.* with a periodic set of flow separations and reattachments. The geometry selected is the same as used in many of the references mentioned above, [6, 7, 9, 10]. The Reynolds number based on the mean bulk velocity and hydraulic diameter is $\mathrm{Re} = 18\,880$ (corresponding to $\mathrm{Re}_\delta = 4\,720$); the three simulated Prandtl numbers are $\mathrm{Pr} = 0.025$, representing lead-bismuth eutectic, $\mathrm{Pr} = 0.2$, which corresponds to a low Prandtl number gaseous mixture, and Pr = 0.71, which corresponds to air. The main characteristics of the velocity field are shown. Results obtained for the temperature fields distribution, the temperature fluctuations, the Nusselt number and the heat fluxes are presented, also considering the Prandtl number effect.

Based on DNS data, and using an *a priori approach*, the accuracy of two widely used models for the representation of turbulent heat fluxes is assessed and discussed. The isotropic model based on the Simple Gradient Diffusion Hypothesis fails in representing the streamwise component of turbulent heat fluxes. In addition it is found that the use of an uniform turbulent Prandtl number might provide inaccurate results when separated flow and shear layers are included in the flow investigated. The Generalized Gradient Diffusion Hypothesis recovers more accurately the direction of turbulent heat fluxes, but it needs to be tuned for the simulation of turbulent heat transfer in Pr $\neq 1$ fluids.

## 1. Governing equations

Governing equations are given in the following in their non-dimensional form. Dimensionless equations are obtained using half the average channel height $\delta$ as the reference quantity for length, $u^* = (\beta\delta/\rho)^{1/2}$ as the reference velocity and $t_{\mathrm{ref}} = \delta/u^*$ as the reference quantity for time. In the definition of the reference velocity, $\rho$ is the density of the fluid and $\beta$ is the constant pressure drop imposed in the $x$ direction, divided by length of the computational domain in streamwise direction

$$\frac{\overline{P}(x,y,z) - \overline{P}(x+L_x,y,z)}{L_x} = \beta \tag{1}$$

Temperature field is made dimensionless using the reference temperature $T_{\mathrm{ref}}$, while a further normalization is performed for allowing for a periodic representation of the temperature, as outlined in section 1.2.

### *1.1. Momentum equation*

For the simulation of the fully developed flow in a channel, the pressure field $P$ is conveniently subdivided into a linear and an unsteady periodic contributions

$$P(x,y,z,t) = -\beta x + p(x,y,z,t) \tag{2}$$

The conservation equations for mass and momentum in dimensionless form result in

$$\nabla \cdot \mathbf{u} = 0 \tag{3}$$

$$\frac{\partial \mathbf{u}}{\partial t} + \nabla \cdot (\mathbf{u} \otimes \mathbf{u}) = -\nabla p + \frac{1}{\mathrm{Re}^*} \nabla^2 \mathbf{u} + \mathbf{b} \tag{4}$$

where $\mathbf{b}$ is the unit vector in $x$ direction, since in the non-dimensional form, $\beta = 1$. $\mathrm{Re}^*$ can be interpreted as the total drag Reynolds number, $\mathrm{Re}^* = u^*\delta/\nu$ and it differs from the friction Reynolds number which is formed using a velocity scale representing only viscous drag effects, $u_\tau = \sqrt{\tau_w/\rho}$.

### *1.2. Energy equation*

Buoyancy effects are neglected in the present study, and the temperature variable $T$ is treated as a passive scalar. Thermophysical properties are assumed to remain constant and viscous dissipation is not accounted for. The non dimensional energy equation with no heat sources, is given by

$$\frac{\partial T}{\partial t} + \nabla \cdot (\mathbf{u}\, T) = \frac{1}{\mathrm{Pe}^*} \nabla^2 T \tag{5}$$

where a still to be defined reference temperature $T_{\mathrm{ref}}$ is used for the non dimensional formulation and $\mathrm{Pe}^* = \mathrm{Re}^*\,\mathrm{Pr}$.

Uniform wall temperature conditions are set at the solid boundaries. A normalization of the temperature field is introduced for simulating the prescribed temperature conditions, by enabling a streamwise periodic variable to be calculated instead of the actual temperature field. While the more common numerical techniques make use of the bulk temperature at every step and an iterative procedure is required for this, the technique employed in this study, directly solves the transport equation of the periodic variable $\theta$

$$\frac{\partial \theta}{\partial t} + \nabla \cdot (\mathbf{u}\, \theta) = \frac{1}{\mathrm{Pe}^*} \nabla^2 \theta + \left( \frac{1}{\mathrm{Pe}^*} \lambda_L^2 + u\, \lambda_L \right) \theta - 2\, \frac{1}{\mathrm{Pe}^*}\, \lambda_L \frac{\partial \theta}{\partial x} \tag{6}$$

with no need of multiple step procedures. The dimensionless, normalized temperature $\theta$ is defined as

$$\theta(x, y, z, t) = \frac{T(x, y, z, t)}{exp(-\lambda_L\, x)} \tag{7}$$

An energy balance is used to evaluate the space averaged temperature decay rate $\lambda_L$ thus closing the system of equations, see Ref. [18]. The effects of axial diffusion are included in the equation for $\lambda_L$ as well as in (6) and are therefore accounted for in the solution. The recovery of the actual temperature field can be finally performed through equation (7).

The temperature-like variable $\theta$ is defined apart from a multiplicative constant associated with the selection of $T_{\rm ref}$ which has been left undetermined up to this point. This is expressed by the following equation

$$\theta(x,y,z,t) = \frac{1}{\widetilde{T}_{\rm ref}} \frac{\widetilde{T}(x,y,z,t)}{exp(-\lambda_L\, x)} \tag{8}$$

where $\widetilde{T}$ indicates the dimensional temperature field. In this work the three $\theta$ fields corresponding to different molecular Pr numbers have been scaled in the post processing phase, and thus also $T_{\rm ref}$ has been selected during post processing so that time and space averaged heat flux at the flat wall equals unity

$$\left.\frac{\partial\theta}{\partial y}\right|_{w,u} = -\mathrm{Pe}^* \tag{9}$$

this allows for immediate comparison between temperature fields at different Pr number and also against results in the literature where heat flux is imposed at the walls. A more detailed description of the method is given in Ref. [18].

### *1.3. Discrete form of the equations*

The Finite Volume code used for the simulations is the same as used in former studies of the flow and heat transfer over corrugated surfaces [19], where the transport equation for the three velocity components are solved by a second order projection-scheme. The Crank-Nicolson scheme is used for the temporal discretization of the diffusive terms of both the momentum and the energy equations, while the Adams-Bashfort scheme is used for the convective terms and for the source term of the energy equation. The spatial discretization is performed by means of second order symmetric schemes. Further details can be found in Ref. [19].

## 2. Computational domain and mesh

### *2.1. Computational domain*

A three dimensional computational domain, periodic in the streamwise direction and homogeneous in the spanwise direction is considered in this

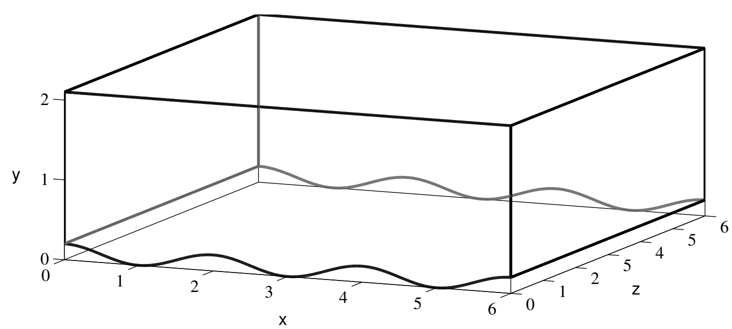


Figure 1: Periodic geometry of the problem, three dimensional view.

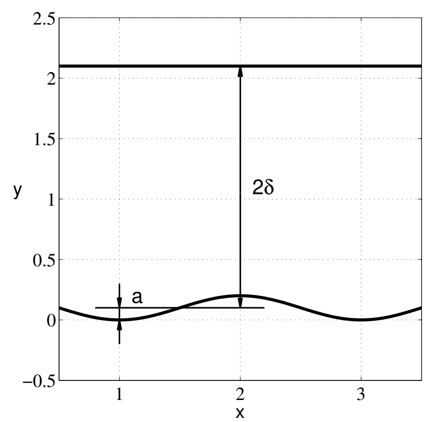


Figure 2: Two dimensional view of the computational domain. The reference length chosen is half the average channel height $\delta$.

study. It is depicted in figure 1, together with the coordinate system. The shape of the wavy wall $y_w$ in the $x$ - $y$ plane is described by

$$y_w = a\left[1 + \cos\left(\frac{2\pi x}{\lambda}\right)\right] \tag{10}$$

where $a$ is the amplitude of the wave and $\lambda$ is the wavelength. In the present investigation wavelength and amplitude are set equal to $2\delta$ and $0.1\delta$ respectively, where $\delta$ corresponds to half the channel average height, see figure 2. Geometrical parameter have been selected to match the geometry investigated in the experiments in Ref. [6] and subsequent DNSs in references [9] and [10].

The size of the domain in streamwise direction is $L_x = 6\delta$; it is smaller than the domain selected by Cherukat *et al.* [10] where computations are performed over four periodicities, but the smaller $L_x$ employed is not expected to affect the accuracy of present results, as demonstrated by the $\lambda_2$ analysis in Ref. [11], which shows that typical large scale structures have size in streamwise direction, $\Lambda_x = \lambda$. The computational domain in the spanwise direction is also $L_z = 6\delta$, *i.e.* 1.5 times larger with respect to Ref. [10] because of the observation of very large spanwise structures ($1.5\lambda$) occurring over wavy walls, as described in Ref. [13].

### *2.2. Computational mesh*

A structured, curvilinear and orthogonal mesh is employed for domain discretization. The number of grid points set for $\mathrm{Re} = 18\,880$ ($\mathrm{Re}_\tau = 282$) is $265 \times 187 \times 221$ along $x$, $y$ and $z$. In order to validate the fluid flow results obtained, a simulation for a Reynolds number of $\mathrm{Re} = 13\,730$ has also been performed on a 253×129×161 mesh. The Reynolds number of this simulation falls very close to the flow regime investigated by Hudson [6] and by Cherukat *et al.* [10] and available in the literature; validation is reported in Appendix A.

| | channel | Re | $\mathrm{Re}_\tau$ | $\Delta x^+$ | $\Delta y^+_{\mathrm{mean}}$ | $y^+_w$ | $\Delta y^+_{\mathrm{max}}$ | $\Delta z^+$ |
|---|---|---|---|---|---|---|---|---|
| Present | wavy | 18 900 | 282 | 6.7 | 3.3 | 0.53 | 5.5 | 7.9 |
| Present | wavy | 13 700 | 216 | 5.3 | 3.6 | 0.58 | 5.7 | 8.3 |
| Ref. [9] | wavy | 11 400 | – | 10.2 | – | 1.6 | 12.4 | 10.2 |
| Ref. [4] | flat | 11 700 | 180 | 9.0 | – | 0.20 | 5.9 | 4.5 |
| Ref. [4] | flat | 27 500 | 395 | 9.9 | – | 0.15 | 6.5 | 4.9 |

Table 1: Grid spacings in wall units. For the purpose of comparison values available in Ref. [4] Ref. [9] are also indicated. Simulations at $\mathrm{Re} = 13\,700$ have been performed for validation, see Appendix A.

Grid spacings for the two Reynolds numbers simulated are given in Table 1. In the same table, details of the mesh used by Kawamura *et al.* [4] for convective heat transfer in a flat channel and in Ref. [9] for the fluid flow over wavy walls are also reported for comparison.

## 3. Non dimensional parameters

In the numerical code employed, the pressure drop at the ends of the channel is imposed through the total drag Reynolds number $\mathrm{Re}^*$ value. The non-dimensional global parameters, the Reynolds number and the friction factor are evaluated in terms of non-dimensional quantities by

$$\mathrm{Re} = 2\mathrm{Re}^*\, Q_s; \qquad f = \frac{4\, H_{\mathrm{av}}}{u_m^2\, Re^*} \left\langle \left| \frac{\partial \overline{u}}{\partial \eta} \right|_w \right\rangle \tag{11}$$

where $Q_s$ is the time-averaged volume flow rate per unit spanwise width of the channel, $2H_{\mathrm{av}}$ corresponds to the average hydraulic diameter, the bulk mean velocity is $u_m \equiv Q_s/H_{\mathrm{av}}$ and the angular brackets indicate a spatial average.

The friction Reynolds number is calculated as

$$\mathrm{Re}_\tau = \frac{u_\tau \delta}{\nu}; \qquad u_\tau = \sqrt{\frac{\tau_{w,u} + \tau_{w,l}}{2\rho}} \tag{12}$$

where the wall shear stress of the upper and lower wall $\tau_{w,u}$ and $\tau_{w,l}$ are calculated on the *projected horizontal area.*

The Nusselt number in terms of non dimensional quantities is evaluated from

$$\langle \mathrm{Nu} \rangle = \frac{2\, H_{\mathrm{av}}}{\langle T_b \rangle - T_w} \left\langle \left| \frac{\partial \overline{T}}{\partial \eta} \right|_w \right\rangle \tag{13}$$

where $\eta$ is the wall normal coordinate.

A local Nusselt number can be defined starting from equation (13)

$$\mathrm{Nu}(x) = \frac{2\, H_{\mathrm{av}}}{T_b - T_w} \left| \frac{\partial \overline{T}}{\partial \eta} \right|_w \tag{14}$$

the local $\mathrm{Nu}(x)$ allows for the discussion of heat transfer performance in specific portions of the channel.

## 4. Results

### *4.1. Velocity field*

Streamlines of the mean velocity field on the periodic module of the channel are depicted in figure 3, together with profiles of the streamwise component of the velocity field. Closer streamlines over the crest of the waves

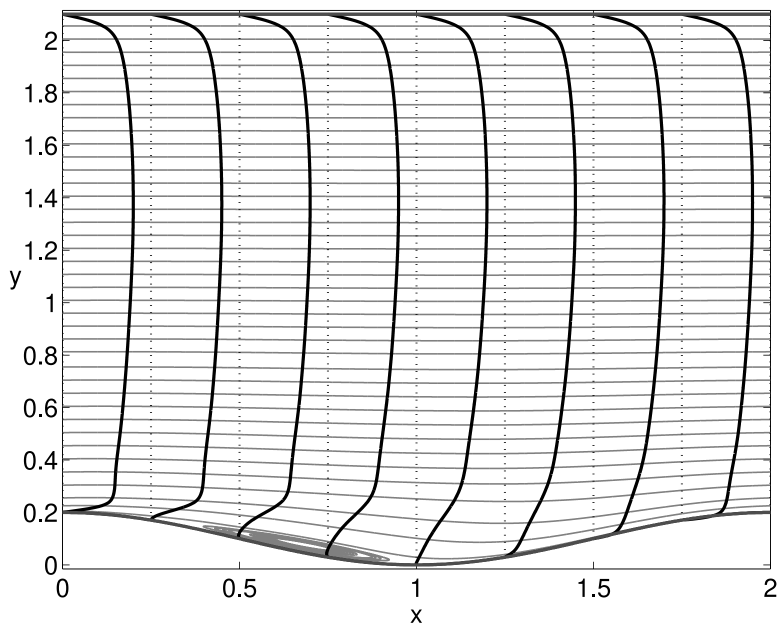


Figure 3: Profiles of the streamwise component of the mean velocity field and streamlines.

indicate flow acceleration; past the crest, the adverse pressure gradient induces flow separation. The thickening of the boundary layer before separation is evident from profiles of $\overline{u}$; a steep velocity gradient at the restart of the boundary layer can also be observed. Peak velocity profiles are located well above the mean channel centerline ($y = 1.1\delta$), this indicates that the influence of the lower wall undulation on the flow field extends beyond half the channel height. Due to the presence of the recirculation bubble in the valleys, viscous drag on the lower wavy wall is smaller with respect to viscous drag calculated on the upper flat wall. The friction factor evaluated through equation (11) gives $f = 0.0247$ at the lower, wavy wall and $f = 0.0345$ at the upper wall. A more complete description and further comments on the friction factors on the flat and the wavy walls are provided in Ref. [20] and also Ref. [10]

Figure 4 shows the root mean square (rms) fluctuation profiles for all three components of the velocity; the behavior is markedly different for different streamwise positions. The region with peak velocity fluctuations is located above the trough and is almost coincident with the shear layer region. The shear layer region is indicated in figure 4 by a gray area where Reynolds

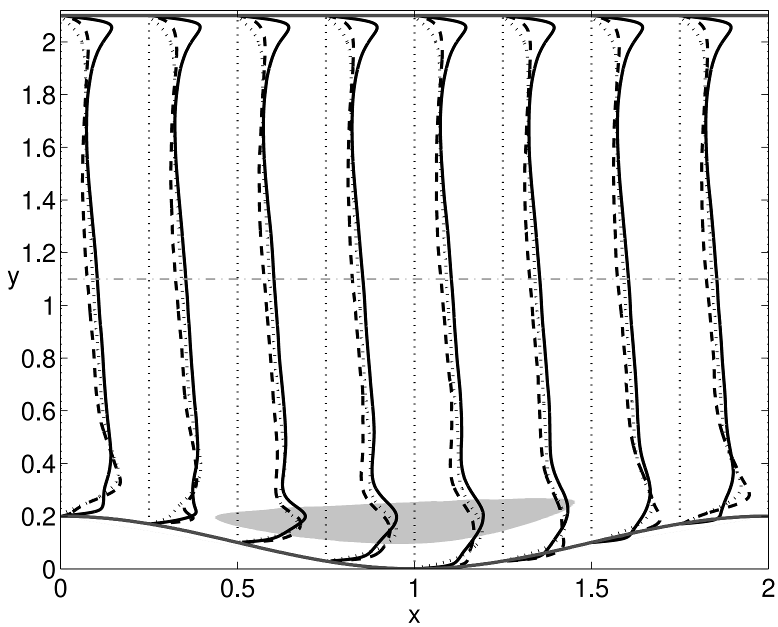


Figure 4: Profiles of the root-mean-square velocity fluctuations. Solid line, $u_{\rm rms}$; dotted line, $v_{\rm rms}$; dashed line, $w_{\rm rms}$. The gray area is the region where Reynolds stress $-\overline{u'v'}$ are greater than 2.1. A gray, horizontal, dashed line indicates the channel centerline $y = 1.1\delta$.

stress exceeds a given threshold $-\overline{u'v'} \geq 2.1$. Despite a global effect of the lower wall undulation is felt by the upper flat wall in terms of larger velocity field fluctuations with respect to the flat channel case (not shown here), fluctuations on the upper wall are essentially independent of the streamwise coordinate. Further details on the flow field characteristics like the Reynolds stress distribution together with the pressure field distribution can be found in previous papers on the turbulent flow in a wavy channel, [7, 10].

### *4.2. Temperature field*

Mean temperature profiles are shown in figure 5. Temperature profiles change their characteristics depending on the Prandtl number: while for Pr = 0.71, the shape of the profile is turbulent, for Pr = 0.025 the profile shape is typically laminar.

Instantaneous contours of the streamwise velocity component and three temperature fields corresponding to the different Prandtl numbers simulated are displayed in figure 6, together with the fluctuation fields. It appears that the mean temperature profiles of laminar characteristics at Pr = 0.025

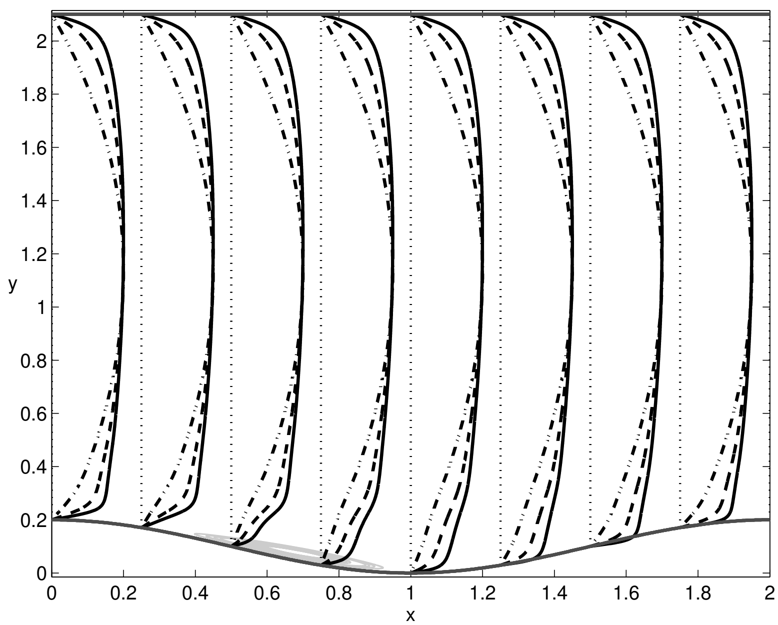


Figure 5: Profiles of the normalized mean temperature field $\theta$ for three different Prandtl number values, solid line: $\mathrm{Pr} = 0.71$; dashed line: $\mathrm{Pr} = 0.20$ and dash-dot line $\mathrm{Pr} = 0.025$. Streamlines of the mean vortex are also indicated in the figure.

shown in figure 5 derive from an unsteady temperature field, a small range of spatial scales and (as discussed later) weak turbulent heat flux in vertical direction. Visual comparison of the $u'$ distribution against temperature fluctuation fields suggest that the calculation of the turbulent diffusivity as the product of the eddy diffusivity and the inverse of a uniform turbulent Prandtl number may not be accurate for $\mathrm{Pr} \ll 1$.

Profiles of the root-mean-square of the temperature fluctuations are depicted in figure 7. Close to the lower wall and for $\mathrm{Pr} = 0.71$ two peaks appear at $x = 0.7$, the lower peak corresponds to the region of maximum velocity of the mean recirculating bubble, while the other one corresponds to the shear layer. Profiles in the boundary layer restart region (see x-stations $x = 1.3$ and $x = 1.7$) display a sharp peak close to the lower wall, while the peak originating from the shear layer is considerably reduced. For $\mathrm{Pr} = 0.025$ it is impossible to discriminate between the two peaks. Shapes of profiles obtained for $\mathrm{Pr} = 0.20$ lie between the two cases discussed.

Turbulent heat fluxes in $x$, $y$ and wall normal direction are depicted in figure 8. Distribution of the turbulent heat fluxes in $x$, figure 8a, reveals

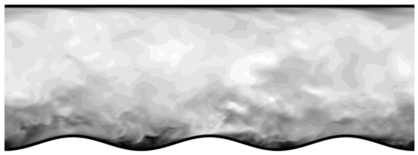

(a) $u$

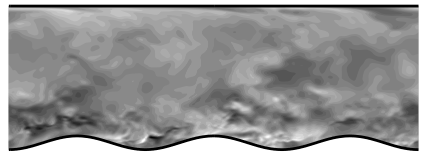

(b) $u'$

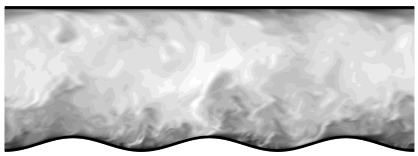

(c) $\theta$ at $\mathrm{Pr} = 0.71$

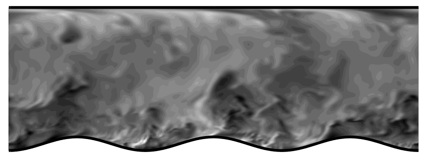

(d) $\theta'$ at $\mathrm{Pr} = 0.71$

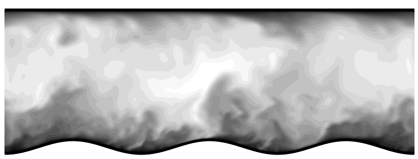

(e) $\theta$ at $\mathrm{Pr} = 0.20$

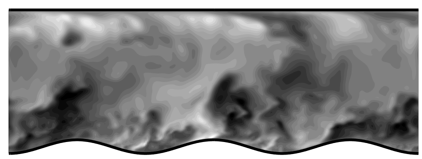

(f) $\theta'$ at $\mathrm{Pr} = 0.20$

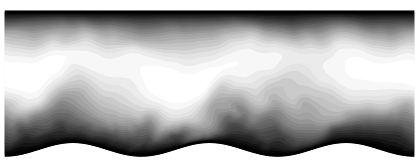

(g) $\theta$ at $\mathrm{Pr} = 0.025$

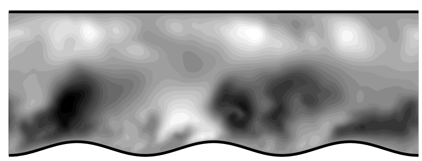

(h) $\theta'$ at $\mathrm{Pr} = 0.025$

Figure 6: Snapshots of the instantaneous streamwise velocity component and temperature fields: $u$ in a; $u'$ in b, $\theta$ in c,e,g; $\theta'$ in d,f,h.

that the streamwise component reaches its maximum along the shear layer region, where Reynolds stress are also large. A very small intensity of turbulent heat fluxes in the flow reattachment region for $(y - y_w)^+ < 15$ can be observed. For decreasing Prandtl numbers, turbulent heat fluxes almost vanish, see figure 8d, this is in direct relation with the laminar shape of mean temperature profiles for $\mathrm{Pr} = 0.025$. Given the turbulent heat fluxes depend on the particular frame of reference employed, figure 8 provides also profiles calculated in a reference frame aligned with the streamlines of the potential flow above the same geometries.

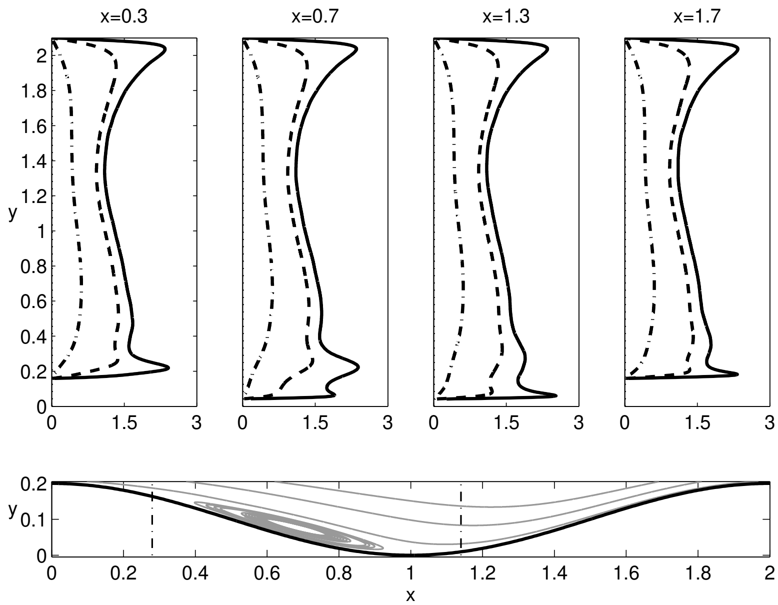


Figure 7: Root-mean-square of the temperature fluctuations, $\theta_{\mathrm{rms}}$, solid line: Pr = 0.71; dashed line: Pr = 0.20 and dash-dot line Pr = 0.025.

#### *4.2.1. Vertical heat fluxes*

Analysis of vertical heat fluxes is used here to examine the heat transport mechanism between the channel walls and the fluid. Vertical heat fluxes can be decomposed into conductive, turbulent and advective contributions

$$q_y = \frac{1}{\mathrm{Re}^*\mathrm{Pr}}\frac{\partial\overline{\theta}}{\partial y} - \overline{v'\theta'} - \overline{v}\overline{\theta} \tag{15}$$

Profiles of the three contributions to $q_y$ and of the total vertical heat flux $q_y$ are presented for the three selected molecular Prandtl numbers in figures 9–11.

The conductive contribution to the heat fluxes in vertical direction is significant in the near wall region; it largely varies along $x$ close to the wavy wall, attaining its minimum close to the separation point, and its maximum past the flow reattachment position. Difference in turbulent heat fluxes in $y$ direction almost vanish for $y \approx 0.4$. Mean advective fluxes are positive or negative, depending on the sign of the mean vertical component of the velocity. Above the lower wall and within the core region not only the mean advective transport in vertical direction $-\overline{v}\overline{\theta}$ is non-negligible, but it prevails

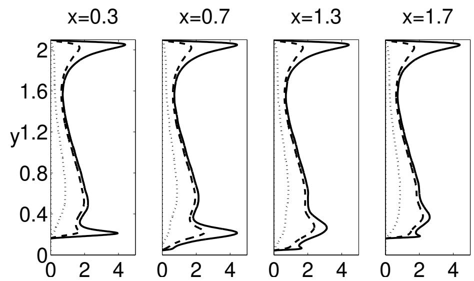


(a) $\overline{u'\theta'}$ at Pr = 0.025, 0.20, 0.71

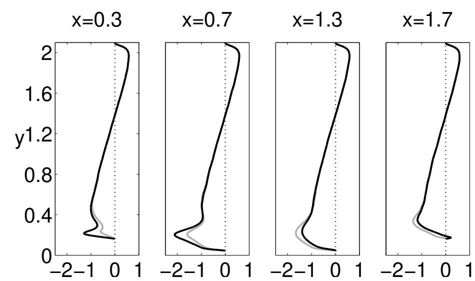


(b) $\overline{v'\theta'}$ at Pr = 0.71

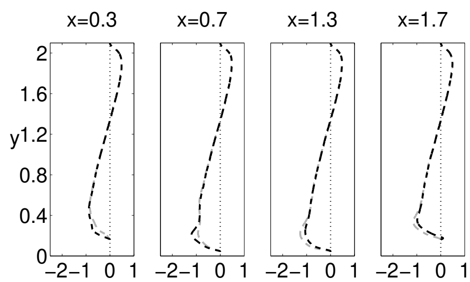


(c) $\overline{v'\theta'}$ at Pr = 0.20

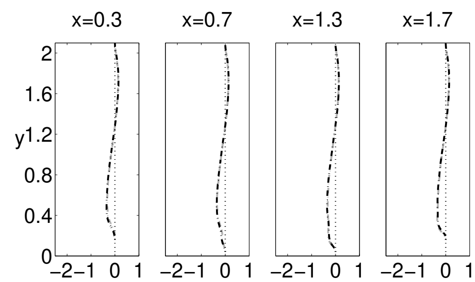


(d) $\overline{v'\theta'}$ at Pr = 0.025

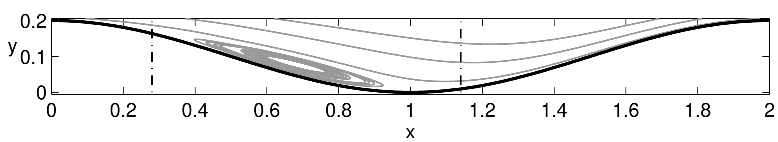


Figure 8: Profiles of turbulent heat fluxes, (a) $\overline{u'\theta'}$: solid line Pr = 0.71; dashed line Pr = 0.20; dash-dot line Pr = 0.025. Insets (b) (c) (d), black lines: vertical heat fluxes; gray lines: heat fluxes calculated on a reference frame locally aligned with the wavy walls.

on turbulent transport, thus representing the main contribution to the vertical heat fluxes. For the lowest Prandtl number investigated, vertical heat fluxes of advective origin, and also total vertical heat fluxes are considerably reduced with respect to the Pr = 0.71 and Pr = 0.20 cases.

#### *4.2.2. Nusselt number*

Local Nusselt numbers, calculated as in equation (14), are displayed in figure 12 for the three fluids considered and for the two channel walls. If by one side heat transfer enhancement at the wavy wall can be ascribed to the presence of flow separation, on the other side heat transfer is hindered

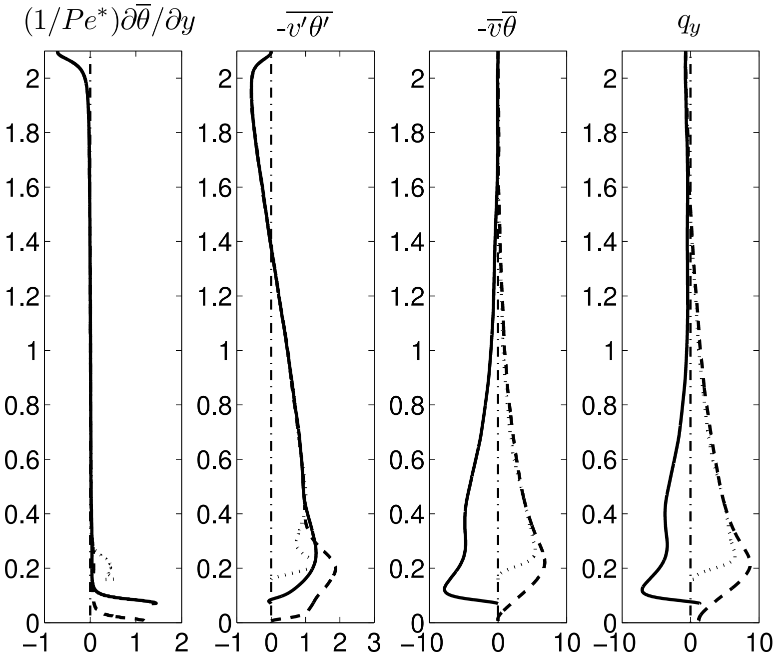


Figure 9: Profiles of the vertical heat fluxes for subsequent axial positions, Pr = 0.71. Dotted line, $x = 0.3$; dashed line, $x = 0.9$; solid line, $x = 1.4$.

by the recirculating bubble; peak heat transfer rate is located in the flow reattachment region. As suggested by results in section 4.2.1, the larger wall heat flux close to reattachment is associated with increased mean advection effects rather than vertical heat fluxes, at least within the present Reynolds number range.

Table 2 reports global Nusselt numbers $\langle \mathrm{Nu} \rangle$ calculated from the present DNS together with Nusselt number values for the flat channel calculated using the correlation by Sleicher and Rouse [21], $\langle \mathrm{Nu} \rangle_f$, and with the heat transfer ratio $h_r$ defined as the ratio between Nusselt numbers of the wavy channels and those of the flat channel, $h_r \equiv \langle \mathrm{Nu} \rangle_c / \langle \mathrm{Nu} \rangle_f$. Given $h_r$ is calculated using a correlation, the ratio between $\mathrm{Nu}(x)$ averaged on the wavy wall and the flat wall of the wavy channel is also provided in table 2, where

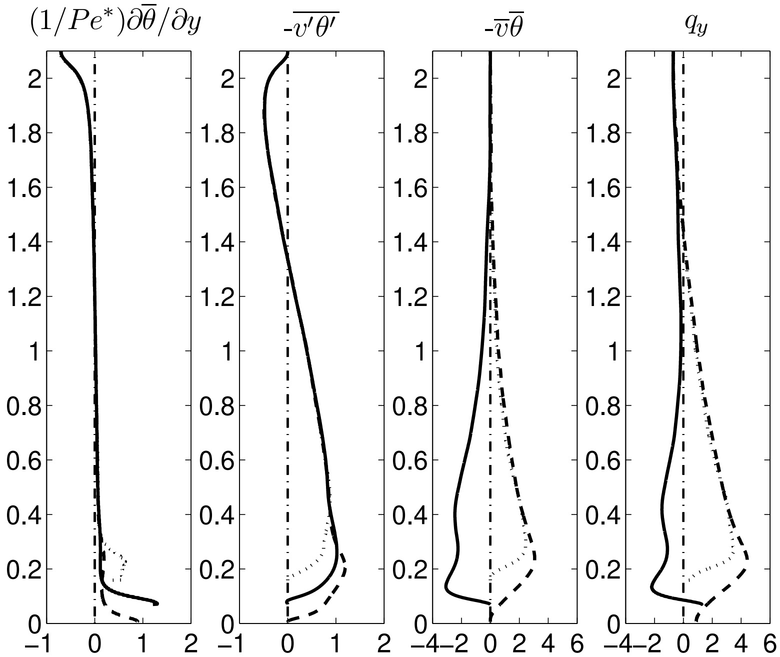


Figure 10: Profiles of the vertical heat fluxes for subsequent axial positions, Pr = 0.20. Dotted line, $x = 0.3$; dashed line, $x = 0.9$; solid line, $x = 1.4$.

it is indicated by $h_{r,w}$.

$$h_{r,w} = \frac{\displaystyle\int_{x=0}^{\lambda} \mathrm{Nu}(x)|_u \,\mathrm{d}x}{\displaystyle\int_{x=0}^{\lambda} \mathrm{Nu}(x)|_l \,\mathrm{d}x} \tag{16}$$

Notice from equations (13) and (14) that unlike the local Nusselt number, the Nusselt of the wavy channel $\langle \mathrm{Nu} \rangle_c$ is calculated using a global bulk temperature and space averaged wall heat fluxes; as a consequence the spatial average of $\mathrm{Nu}(x)$ at the two walls may very well not correspond to the global $\langle \mathrm{Nu} \rangle_c$.

The Nusselt number of low Prandtl number fluids is low. Heat transfer enhancement due to the presence of the wavy wall is instead substantial. The ratio between Nusselt numbers at the two walls $h_{r,w}$ is seen to decrease for decreasing Pr. The heat transfer enhancement obtained is compensated by a corresponding increase in friction drag, and in the addition of a form drag

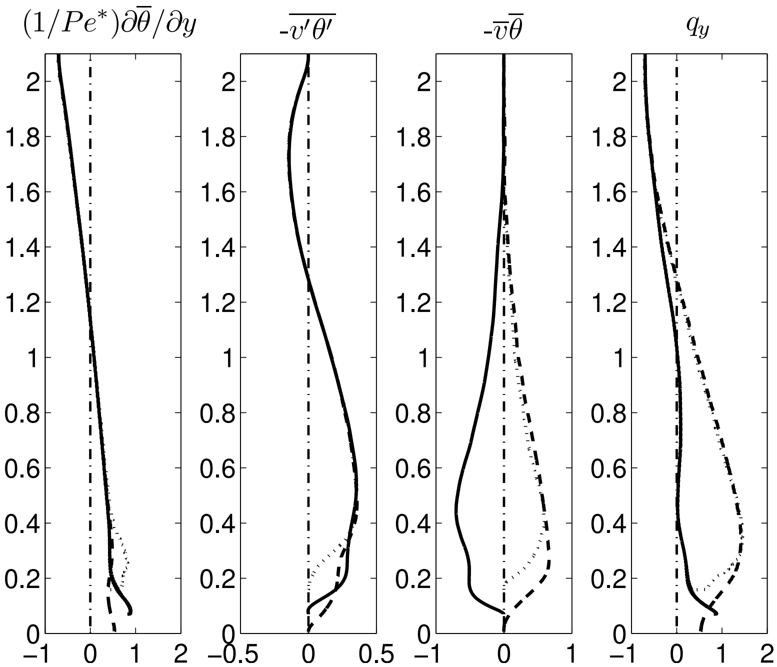


Figure 11: Profiles of the vertical heat fluxes for subsequent axial positions, Pr = 0.025. Dotted line, $x = 0.3$; dashed line, $x = 0.9$; solid line, $x = 1.4$.

whose measure is in the difference between the total drag velocity $u^*$ and the friction velocity $u_\tau$.

| Pr | $\langle \mathrm{Nu} \rangle_f$ (Ref. [21]) | $\langle \mathrm{Nu} \rangle$ (present) | $h_r$ | $h_{r,w}$ | $\langle \mathrm{Pr}_t \rangle$ (present) |
|---|---|---|---|---|---|
| 0.71 | 47 | 77.3 | 1.64 | 1.57 | 0.861 |
| 0.20 | 19 | 37.1 | 1.95 | 1.46 | 0.924 |
| 0.025 | 7.3 | 12.2 | 1.67 | 1.17 | 1.22 |

Table 2: Space averaged Nusselt numbers, heat transfer ratio and $\mathrm{Pr}_t$ at Re = 18 880 .

### *4.3. Turbulent Prandtl number distribution*

The turbulent Prandtl number is a fundamental parameter for practical heat transfer analyses. It is often defined as a scalar, with the wall normal

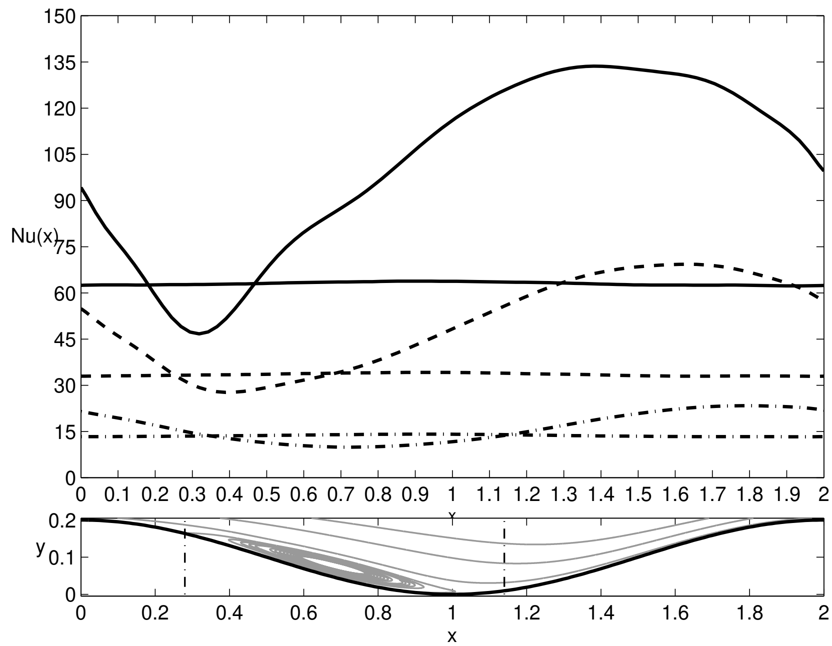


Figure 12: Profiles of the local Nusselt number: curves are for the lower wall while the almost horizontal lines are for the upper, flat wall. The solid line indicates $\mathrm{Nu}(x)$ for $\mathrm{Pr} = 0.71$, the dashed line is for $\mathrm{Pr} = 0.20$, the dash-dot line for $\mathrm{Pr} = 0.025$.

direction selected as the direction of the main heat fluxes

$$\mathrm{Pr}_t \equiv \frac{\overline{u'v'}\ \dfrac{\partial\overline{\theta}}{\partial y}}{\overline{v'\theta'}\ \dfrac{\partial\overline{u}}{\partial y}} \tag{17}$$

The assumption of a uniform value of $\mathrm{Pr}_t$ is included in the hypothesis of most turbulence models for the closure of RANS equations. This is also the case of the Simple Gradient Diffusion Hypothesis (SGDH), which is probably the most widely used turbulent heat flux model.

Contour plots of the turbulent Prandtl number calculated from equation (17) are shown in figure 13 and compared to contour plots of vertical heat fluxes. In insets a), c), e) gray levels indicate $0.50 < \mathrm{Pr}_t < 3.3$, the local $\mathrm{Pr}_t$ value is instead beyond those limits in white regions. This allows to emphasize regions where the local $\mathrm{Pr}_t$ exceeds the range of the expected values before a possible divergence $\mathrm{Pr}_t \to \pm\infty$.

As opposed to the flat channel case, where $\mathrm{Pr}_t$ diverges about the channel centerline, in the present case unboundedness is observed also close to the walls. This is not surprising as in a separation bubble the $\partial\overline{u}/\partial y$ derivative becomes zero at least once for each $x$-coordinate. In addition, in the wavy channel of the present investigation $\overline{v'\theta'}$ approaches zero in the upslope portion of the domain for $y^+ < 20$. A small turbulent mixing in vertical direction is due to favorable pressure gradient and a concave streamline shape, which, as investigated in [22], locally inhibits vertical fluctuations.

There are many physical cases where the turbulent Prandtl number diverge also close to the solid walls, the comparison between turbulent Prandtl number distributions and vertical heat fluxes in figure 13 suggests that in these cases $\mathrm{Pr}_t$ cannot provide a reliable approximation to the turbulent heat fluxes.

Space averages of the turbulent Prandtl number are given in table 2 using data of the present DNS; as there are regions in the field where the local $\mathrm{Pr}_t \to \pm\infty$, these are evaluated omitting from the calculation all computational cells where $\mathrm{Pr}_t < 0.50$ or $\mathrm{Pr}_t > 3.3$.

### *4.4. Turbulent convection modeling in a wavy channel*

In this paragraph, results obtained from the DNS are used as reference data for assessing the accuracy of turbulent heat fluxes predicted by the SGDH model in the present geometry and conditions, thus performing an *a priori* analysis of the model. Further in the discussion, the possible application of a Generalized Gradient Diffusion Hypothesis (GGDH) in modeling turbulent heat transfer over wavy walls will be evaluated, with special attention on direction of the modeled turbulent stress, application to fluids of different Prandtl numbers and application on moderately complex geometries.

The SGDH model is based on the gradient diffusion hypothesis

$$\overline{u_i'T'} = -\frac{\nu_t}{\widehat{\mathrm{Pr}}_t}\frac{\partial\overline{T}}{\partial x_i} \tag{18}$$

where $\widehat{\mathrm{Pr}}_t$ indicates an assigned value for the turbulent Prandtl number. In order to single out errors associated with turbulent transport modeling, DNS data are used in equation (18) for both temperature gradient and eddy viscosity to form the modeled heat fluxes.

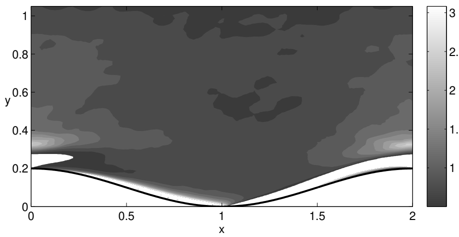


(a) $\mathrm{Pr}_t$ for $\mathrm{Pr} = 0.71$

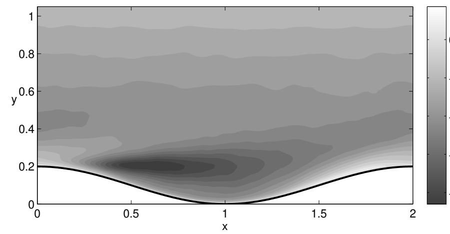


(b) $\overline{v'\theta'}$ at $\mathrm{Pr} = 0.71$

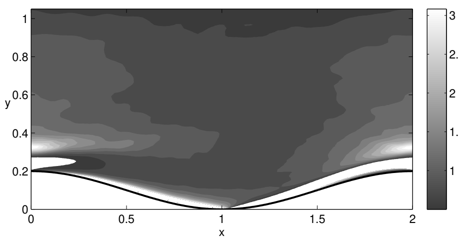


(c) $\mathrm{Pr}_t$ for $\mathrm{Pr} = 0.20$

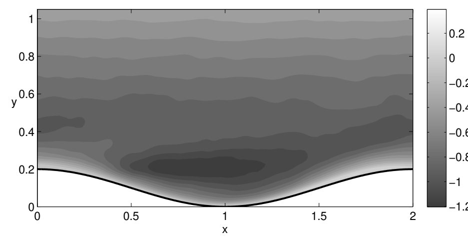


(d) $\overline{v'\theta'}$ at $\mathrm{Pr} = 0.20$

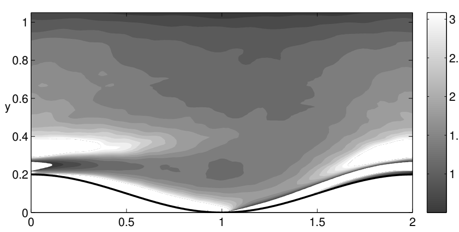


(e) $\mathrm{Pr}_t$ for $\mathrm{Pr} = 0.025$

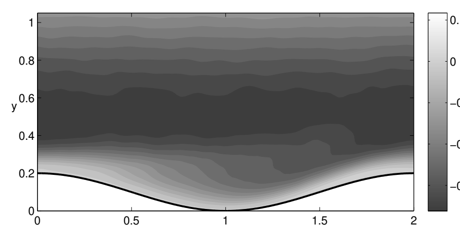


(f) $\overline{v'\theta'}$ at $\mathrm{Pr} = 0.025$

Figure 13: Contour plots of the time-averaged turbulent Prandtl number over the wavy walls are displayed in insets (a), (c), (e). White regions indicate $\mathrm{Pr}_t < 0.50$ or $\mathrm{Pr}_t > 3.3$. Insets (b), (d), (f) display contour plots of the time-averaged vertical heat fluxes. Values of $\langle \mathrm{Pr}_t \rangle$ for the three molecular Pr are given in table 2.

Figure 14 displays turbulent heat flux vectors from DNS and from the SGDH model using $\widehat{\mathrm{Pr}_t} = 0.9$. Given the isotropic character of the gradient diffusion hypothesis, the model fails to represent the streamwise component of turbulent heat fluxes, see also Ref. [20]. In particular it fails in taking into account that while turbulent fluxes are substantial in the streamwise direction (a couple of times larger than turbulent heat fluxes in the wall normal direction), the time-averaged temperature derivative in $x$ is very small (about one order of magnitude smaller than $\partial T/\partial \eta$). As a consequence the

SGDH only gives a fair indication of the turbulent heat flux in the wall normal direction, along which the turbulent Prandtl number has been calculated, see also Launder [23].

It is apparent in this context that resorting to a anisotropic turbulent heat flux model could improve the quality of the representation of turbulent heat fluxes. The Generalized Gradient Diffusion Hypothesis (GGDH), which inherits his anisotropy from the Reynolds Stress tensor, is often employed in complex flow configurations. When the flow is homogeneous in $z$ as in the channel with wavy walls, the simplest form of the GGDH model writes

$$\begin{aligned} \overline{u'T'} &= C_\theta \tau_c \left( \overline{u'^2} \frac{\partial \overline{T}}{\partial x} + \overline{u'v'} \frac{\partial \overline{T}}{\partial y} \right) \\ \overline{v'T'} &= C_\theta \tau_c \left( \overline{u'v'} \frac{\partial \overline{T}}{\partial x} + \overline{v'^2} \frac{\partial \overline{T}}{\partial y} \right) \\ \overline{w'T'} &= 0 \end{aligned} \tag{19}$$

where $C_\theta$ is a model constant ($C_\theta = 0.3$), and $\tau_c$ is the characteristic time-scale distribution $\tau_c = \tau_c(x, y)$. The GGDH turbulent convection model is meant to be coupled with the use of a model for the full Reynolds stress tensor.

Given that in the GGDH model equation $\tau_c$, although based on mechanical quantities $\tau_c = k/\varepsilon$ in the customary implementations (see [24]), is primarily responsible for the *module* of the turbulent heat flux vector for all Prandtl numbers, the assessment of the GGDH model is split into two separate stages.

- First the *direction* of the modeled turbulent heat flux vector –which does not depend on the $C_\theta \tau_c$ product– is investigated;
- secondly $C_\theta \tau_c$ is calculated form DNS quantities, allowing in this way to investigate to which extent the time scale $\tau_c$ can be considered as independent of the Prandtl number.

A more direct approach like for example the evaluation of $\tau_c$ from $k$ and $\varepsilon$ extracted from DNS results, would introduce the supplementary uncertainty associated with the correct representation of the turbulent kinetic energy dissipation rate $\varepsilon$, whose transport equation is heavily modeled and whose distribution computed in a RANS simulation framework is typically very different form the $\varepsilon$ which would be calculated by substitution of quantities extracted from a DNS directly into its definition.

Figure 15 displays unit vectors directed like turbulent heat fluxes calculated by DNS, and by the two models: SGDH and GGDH. The improvement in the representation by GGDH of the turbulent flux direction is apparent; the accuracy in the determination of the module of the vector depends instead on the calculation of the local time scale distribution.

Figures 16 and 17 display the $C_\theta \tau_c$ product calculated from equation (19) through an *a priori* approach, where all turbulent flow statistics and temperature derivatives are provided by DNS data and *the module* of the modeled turbulent heat flux vector is compared to the module of the calculated turbulent heat flux vector to get the $C_\theta \tau_c$ distribution.

In figure 16, data are averaged in time, along $x$ and along $z$ and for this reason, the profile is shown only far enough ($y - y_w \gtrapprox 0.7$) from the wavy wall. From the inspection of figure 16 it can be concluded that a dependence of $C_\theta$ from the molecular diffusivity of the fluid is non negligible for fluids of molecular Prandtl numbers of $\mathcal{O}(10^{-1})$ or $\mathcal{O}(10^{-2})$.

Figure 17 displays the $C_\theta \tau_c$ product close to the wavy walls. The $C_\theta \tau_c$ values are averaged in time and the spanwise direction only, for two different molecular Prandtl numbers and for two different $x$ locations: valley of the wave and crest of the wave. The $\mathrm{Pr} = 0.71$ case is not displayed in the figure for clarity, as if by one side the time scale value do not differ appreciably from the $\mathrm{Pr} = 0.2$ case, on the other side the profile is less regular. It can be concluded that for moderately complex wall geometries, also involving separation, the product $C_\theta \tau_c$ is rather independent of the location where it is calculated, thus encouraging its use over moderately complex geometries.

## 5. Conclusions

Forced convective heat transfer is simulated by DNS in an infinite channel with one wavy wall and one flat wall. The simulated friction Reynold number is $\mathrm{Re}_\tau = 282$, corresponding to a Reynold number of the bulk velocity and the hydraulic diameter, $\mathrm{Re} \approx 18\,900$. Heat transfer is simulated for three fluids of different thermal conductivity, corresponding to $\mathrm{Pr} = 0.71, 0.20, 0.025$. As the fluid flow features in the same geometries and for the same Reynolds number range has been extensively investigated numerically and through experiments, only few results are provided concerning the fluid flow features.

Profiles of turbulent heat flux show that for the Reynolds number of our simulations, turbulent heat flux almost vanish at $\mathrm{Pr} = 0.025$; as a consequence mean temperature profiles at those low Péclet number values are typically laminar. Also temperature fluctuations are very different depending on the thermal diffusivity of the flow. A peak observed on $\theta_{\mathrm{rms}}$ for $\mathrm{Pr} = 0.71$ corresponding to the shear layer region is almost indistinguishable in the very low Prandtl number range.

As expected, low Prandtl number fluids are characterized by comparatively low Nusselt numbers but heat transfer is enhanced by the wall undulation. While heat transfer is minimum in the separated flow region, where the recirculating bubble act as a barrier to the advection of heat, a peak heat transfer rate is found in the flow reattachment region for all fluids investigated. A detailed investigation of the components of heat flux in vertical direction reveals that the main contribution to heat transfer is always to be ascribed to the *mean advective term*, at least within the range of parameters investigated.

Two widely used models of turbulent heat fluxes are evaluated through an *a priori* approach. The model based on the Simple Gradient Diffusion Hypothesis uses the turbulent Prandtl number for turbulent heat transfer predictions. While the dependence of $\mathrm{Pr}_t$ on the molecular Prandtl number has been extensively investigated in the literature, it is shown in this work that separation and in general complex flow configuration can have even more severe effects on the turbulent Prandtl number distribution. Further, the SGDH model is shown to fail in the prediction of turbulent heat fluxes in the streamwise direction, for $\mathrm{Pr} \sim 1$ and low Prandtl number fluids, for flow configurations including separated flow as well as in flat geometries. In summary the direction of the turbulent heat fluxes is misrepresented by the SGDH model. The direction of turbulent heat fluxes is predicted more accurately by the the GGDH model. On the other hand, given the time scale included in the model is a mechanical quantity, the $C_\theta$ constant should be modified to take into account the thermal diffusivity of the fluid simulated, when the Prandtl number of the simulated fluid is far from $\mathrm{Pr} \approx 1$


## Acknowledgements

This research is funded by THINS, a European funded large-scale collaborative project within the VII Framework Program (project number 249337).

## Appendix A. Validation of fluid flow results

In this section, fluid flow results are validated against experimental data available from Ref. [6] and DNS data from Ref. [10]. In order to match the Reynolds number of reference data, Re = 13 840 validation is performed using the same code as discussed in section 1 but for a smaller Reynolds number Re = 13 700 with respect to the turbulent heat transfer results presented and a coarser mesh, see Table 1.

Figure A.18 displays all comparisons performed. Profiles of the mean velocity field in horizontal and vertical direction, together with the root-mean-square velocity fluctuations are compared to data available and taken directly from figures 10a and 10b in Ref. [10]. In summary it can be concluded that the fluid flow predicted by the present simulations compare well against both experiments and numerical simulations available in the literature.

## References


[1] H. Kawamura, K. Ohsaka, H. Abe, K. Yamamoto, DNS of turbulent heat transfer in channel flow with low to medium-high Prandtl number fluid, Int. J. Heat Fluid Flow 19 (1998) 482–491.

[2] H. Kawamura, H. Abe, Y. Matsuo, DNS of turbulent heat transfer in channel flow with respect to Reynolds and Prandtl number effects, International Journal of Heat and Fluid Flow 20 (3) (1999) 196–207.

[3] M. Piller, E. Nobile, T. Hanratty, DNS study of turbulent transport at low Prandtl numbers in a channel flow, J. Fluid Mech. 458 (2002) 419–441.

[4] H. Kawamura, H. Abe, Y. Matsuo, Surface heat-flux fluctuation in a turbulent channel flow up to $\mathrm{Re}_\tau = 1020$ with Pr = 0.025 and 0.71, Int. J. Heat Fluid Flow 25 (2004) 404–419.

[5] D. Zilker, T. Hanratty, Influence of the amplitude of a solid wavy wall on a turbulent flow. Part 2. separated flows, J. Fluid Mech. 90 (1979) 257–271.

[6] J. D. Hudson, The effect of a wavy boundary on turbulent flow, Ph.D. thesis, University of Illinois (1993).

[7] J. D. Hudson, L. Dykhno, T. J. Hanratty, Turbulence production in flow over a wavy wall, Experiments in Fluids 20 (1996) 257–265.

[8] S. Kuhn, C. Wagner, P. R. von Rohr, The influence of wavy walls on the transport of a passive scalar in turbulent flows, Journal of Turbulence 9 (10) (2008) 1–17.

[9] C. Maaß, U. Schumann, Direct numerical simulation of separated turbulent flow over a wavy boundary, in: E. H. Hirschel (Ed.), Flow simulation with high-performance computers, Vieweg, DLR, Institut fur Physik der Atmosphare D-82230 Oberpfanffenhofen, Germany, 1996.

[10] P. Cherukat, Y. Na, T. J. Hanratty, Direct numerical simulation of a fully developed turbulent flow over a wavy wall, Theoret. Comput. Fluid Dynamics 11 (1998) 109–134.

[11] R. J. Calhoun, R. L. Street, Turbulent flow over a wavy surface: Neutral case, J. Geophys. Res. 106 (2001) 9277–9293.

[12] V. Patel, J. Cohn, J. Yoon, Turbulent flow in a channel with a wavy wall, Journal of Fluids Engineeering 113 (1991) 579–586.

[13] A.Günther, P. R. von Rohr, Structure of the temperature field in a flow over a heated waves, Experiments in Fluids 33 (2002) 920–930.

[14] A. Z. Dellil, A. Azzi, B. A. Jubran, Turbulent flow and convective heat transfer in a wavy wall channel, Heat and Mass Transfer 40 (2004) 793–799.

[15] H. S. Choi, K. Suzuki, Large eddy simulation of turbulent flow and heat transfer in a channel with one wavy wall, Int. J. Heat Fluid Flow 26 (2005) 681–694.

[16] R. Rossi, Passive scalar transport in turbulent flows over a wavy walls, Ph.D. thesis, Università degli studi di Bologna (2006).

[17] R. Rossi, A numerical study of algebraic flux models for heat and mass traansport simulation in complex flows, Int. J. Heat Mass Transfer 53 (2010) 4511–4524.

[18] E. Stalio, M. Piller, Direct numerical simulation of heat transfer in converging-diverging wavy channels, ASME Journal of Heat Transfer 129 (7) (2007) 769–777.

[19] E. Stalio, E. Nobile, Direct numerical simulation of heat transfer over riblets, Int. J. Heat Fluid Flow 24 (2003) 356–371.

[20] O. Errico, E. Stalio, Direct numerical simulation of turbulent forced convection in a wavy channel at low and order one Prandtl number, International Journal of Thermal Sciences 86 (2014) 374–386.

[21] C. A. Sleicher, M. W. Rouse, A convenient correlation for heat transfer to constant and variable property fluids in turbulent pipe flow, Int. J. Heat Mass Transfer 18 (1975) 667–683.

[22] R. N. Meroney, P. Bradshaw, Turbulent boundary-layer growth over a longitudinally curved surface, aiaaj 13 (1975) 1448–1453.

[23] B. E. Launder, Rans modelling of turbulent flows affected by buoyancy or stratification, in: G. Hewitt, J. Vassilicos (Eds.), Prediction of turbulent flows, Cambridge University Press, Cambridge, 2005.

[24] B. J. Daly, F. H. Harlow, Transport equations in turbulence, Phys. Fluids 13 (1970) 2634–2649.

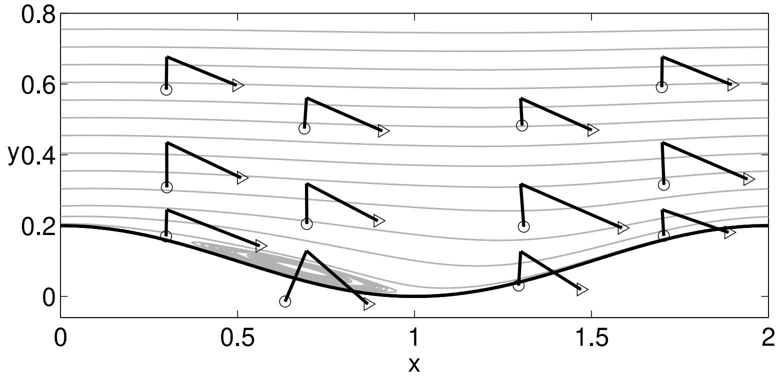


(a) Pr = 0.71

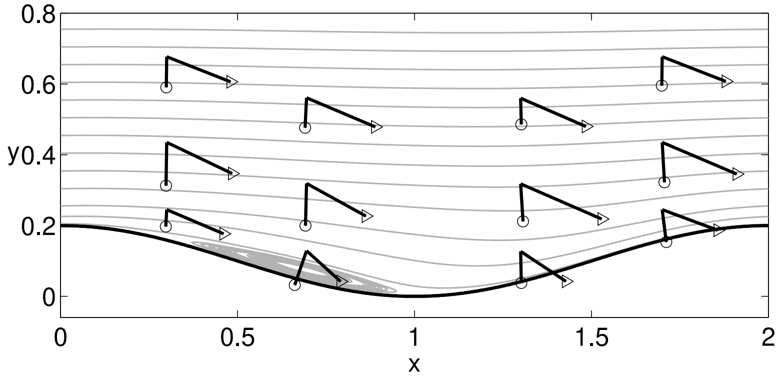


(b) Pr = 0.20

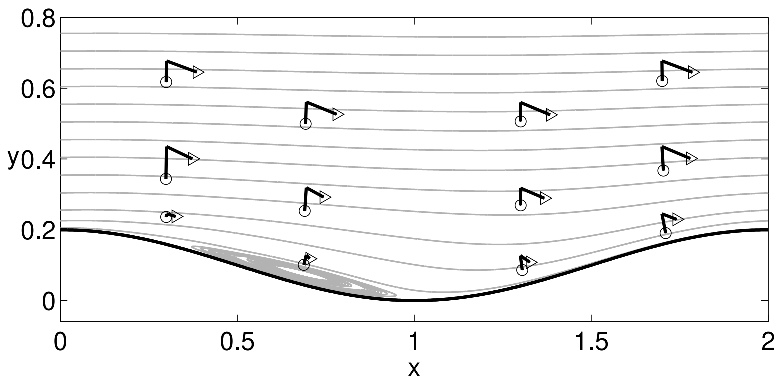


(c) Pr = 0.025

Figure 14: Comparison between vectors of turbulent heat fluxes, for the three different Pr. Triangle head: DNS results; round head: SGDH model using $\widehat{\mathrm{Pr}}_t = 0.9$ for all Prandtl numbers.

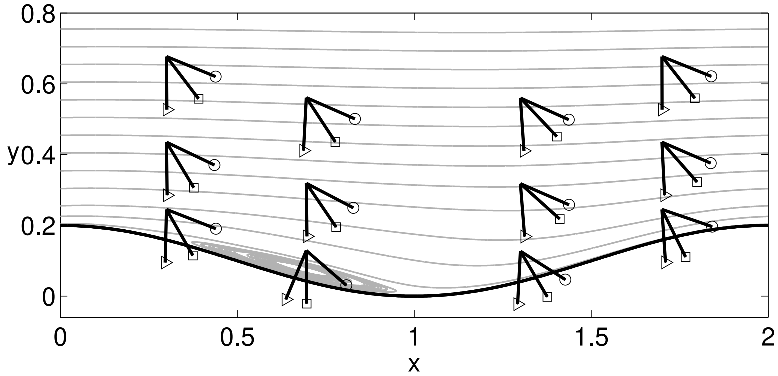


(a) Pr = 0.71

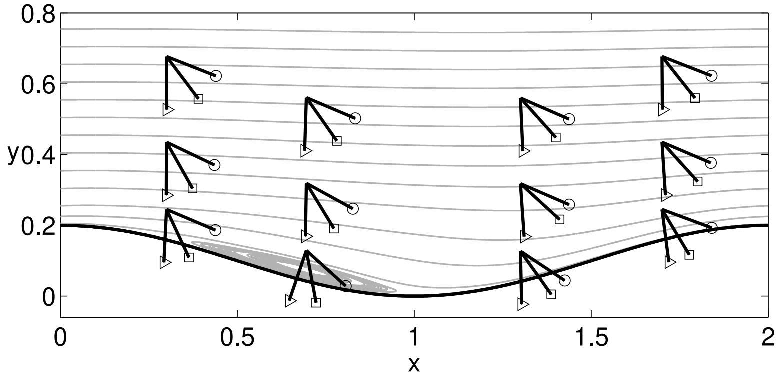


(b) Pr = 0.20

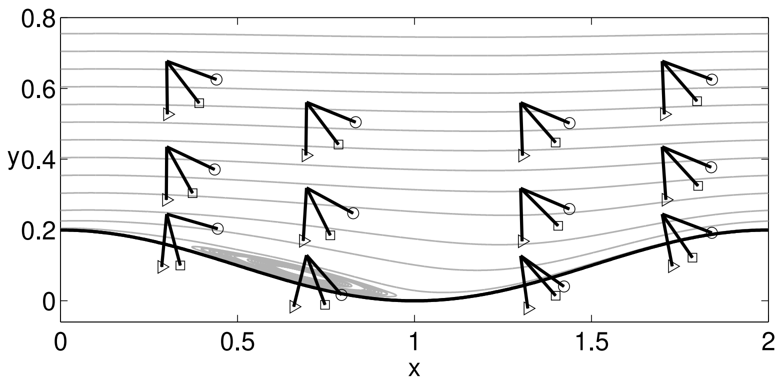


(c) Pr = 0.025

Figure 15: Unit vectors of the turbulent heat fluxes, (a) Pr = 0.71; (b) Pr = 0.20; (c) Pr = 0.025. Circle arrows head for DNS results, square arrows head for the GGDH model, triangle arrows head for the SGDH.

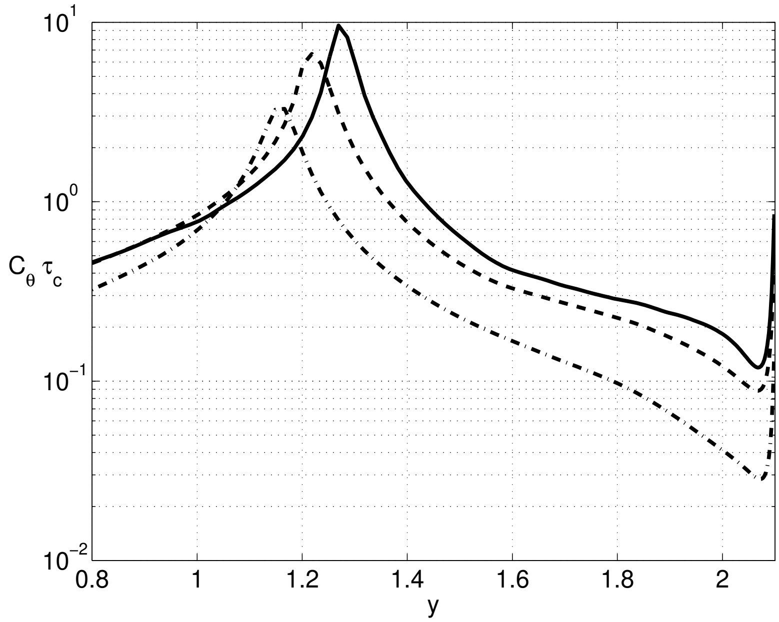


Figure 16: Time, $x$ and $z$ average of the $C_\theta \tau_c$ product for $y - y_w \gtrapprox 0.7$ and for three different Prandtl number values, solid line: Pr = 0.71; dashed line: Pr = 0.20 and dash-dot line Pr = 0.025.

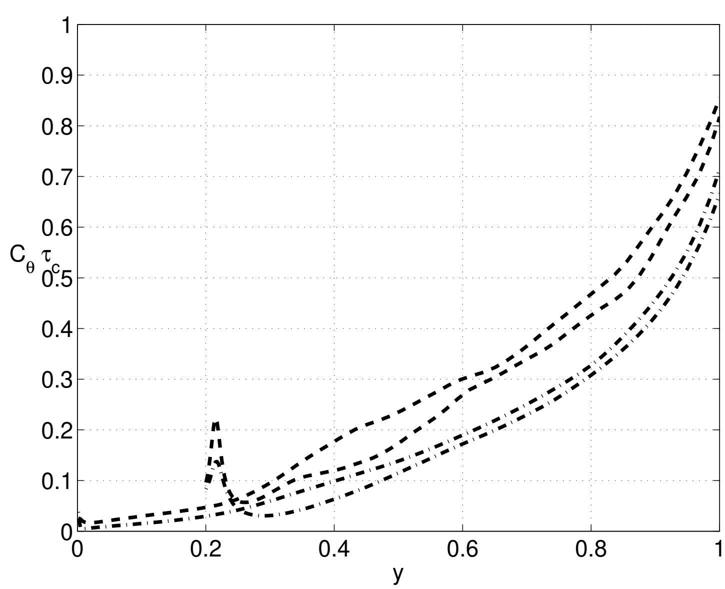


Figure 17: Time and $z$ average of the $C_\theta \tau_c$ product for $y - y_w \lessapprox 0.9$ and for two different Prandtl number values; dashed line: Pr = 0.20 and dash-dot line Pr = 0.025.

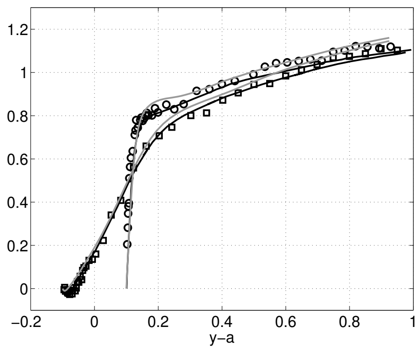


(a) $\dfrac{u}{u_m}$

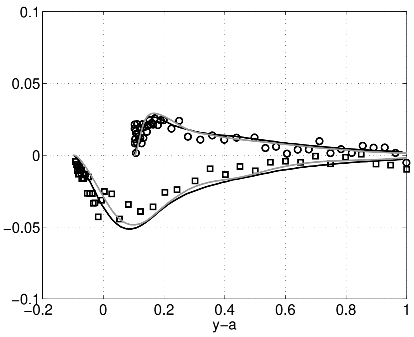


(b) $\dfrac{v}{u_m}$

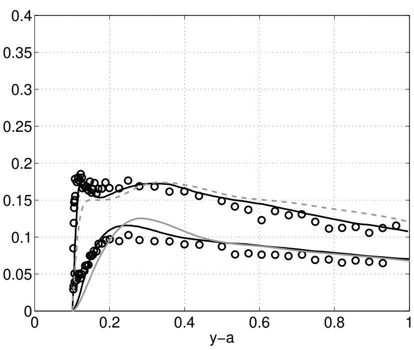


(c) $\dfrac{u_{\mathrm{rms}}}{u_m}, \dfrac{v_{\mathrm{rms}}}{u_m}$

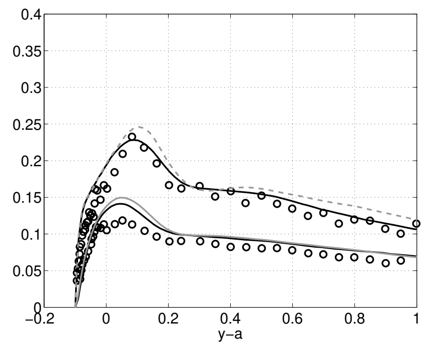


(d) $\dfrac{u_{\mathrm{rms}}}{u_m}, \dfrac{v_{\mathrm{rms}}}{u_m}$

Figure A.18: Validation of the numerical technique employed by comparison with experiments and DNS results from the literature. (a) Profiles of the normalized mean streamwise velocity for crest and trough. Gray lines indicate present results; symbols indicate measurements in Ref. [6]; solid black lines are for the DNS in Ref. [10]. (b) Profiles of the normalized mean vertical velocity for crest and trough. Legend is like for figure A.18a. (c) Profiles of the normalized root-mean-square velocity fluctuations at the crest. The dashed gray line indicates $u_{\mathrm{rms}}/u_m$, the solid gray line is for $v_{\mathrm{rms}}/u_m$; symbols indicate measurements in Ref. [6]; dashed lines are for the DNS in Ref. [10]. (d) Profiles of the normalized root-mean-square velocity fluctuations at the trough; legend is like for figure A.18c

.